



Article

High-Resolution Monitoring of Tidal Systems Using UAV: A Case Study on Poplar Island, MD (USA)

Yuri Taddia ^{1,2,*} , Alberto Pellegrinelli ¹ , Corinne Corbau ², Giulia Franchi ³, Lorie W. Staver ², John Court Stevenson ² and William Nardin ²

¹ Engineering Department, University of Ferrara, Via Saragat 1, 44122 Ferrara, Italy; alberto.pellegrinelli@unife.it

² Horn Point Laboratory, University of Maryland Center for Environmental Science, 2020 Horns Point Road, Cambridge, MA 21613, USA; ccorbau@umces.edu (C.C.); lstaver@umces.edu (L.W.S.); court@umces.edu (J.C.S.); wnardin@umces.edu (W.N.)

³ Department of Mathematics and Computer Science, Salisbury University, 1101 Camden Avenue, Salisbury, MD 21801, USA; gxfranchi@salisbury.edu

* Correspondence: yuri.taddia@unife.it; Tel.: +39-0532-974918

Abstract: Tidal processes regulating sediment accretion rates and vegetated platform erosion in tidal systems strongly affect salt marsh evolution. A balance between erosion and deposition in a restored salt marsh is crucial for analyzing restoration strategies to be adopted within a natural context. Marsh morphology is also coupled with tidal mudflats and channel networks and this makes micro-tidal systems crucial for a detailed assessment of restoration interventions. Here, we present a methodological approach for monitoring channel morphodynamics and vegetation variations over a time frame of six years in a low tidal energy salt marsh of the Paul S. Sarbanes Ecosystem Restoration Project at Poplar Island (Maryland, USA). The project is a restoration site where sediment dredged from the shipping channels in the upper Chesapeake Bay is used to restore a tidal marsh habitat in mid-Chesapeake Bay. Aerial surveys with an Unmanned Aerial Vehicle (UAV) have been performed for the high-resolution mapping of a small tidal system. Flight missions were planned to obtain a Ground Sample Distance (GSD) of 2 cm. Structure-from-Motion (SfM) and Multi-View-Stereo (MVS) algorithms have been used to reconstruct the 3D geometry of the site. The mapping of channel morphology and an elevation assessment on the mudflat were performed using orthomosaics, Digital Terrain Models (DTMs) and GNSS survey. The results highlight that the workflow adopted in this pilot work is suitable to assess the geomorphological evolution over time in a micro-tidal system. However, issues were encountered for salt marsh due to the presence of dense vegetation. The UAV-based photogrammetry approach with GNSS RTK ground surveys can hence be replicated in similar sites all over the world to evaluate restoration interventions and to develop new strategies for a better management of existing shorelines.

Keywords: Unmanned Aerial Vehicle (UAV); salt marsh restoration; micro-tidal system; high-resolution monitoring; coastal geomorphology



Citation: Taddia, Y.; Pellegrinelli, A.; Corbau, C.; Franchi, G.; Staver, L.W.; Stevenson, J.C.; Nardin, W. High-Resolution Monitoring of Tidal Systems Using UAV: A Case Study on Poplar Island, MD (USA). *Remote Sens.* **2021**, *13*, 1364. <https://doi.org/10.3390/rs13071364>

Academic Editors: Alberto Canestrelli, Sergio Marconi and Alvise Finotello

Received: 2 March 2021

Accepted: 31 March 2021

Published: 2 April 2021

Publisher's Note: MDPI stays neutral with regard to jurisdictional claims in published maps and institutional affiliations.



Copyright: © 2021 by the authors. Licensee MDPI, Basel, Switzerland. This article is an open access article distributed under the terms and conditions of the Creative Commons Attribution (CC BY) license (<https://creativecommons.org/licenses/by/4.0/>).

1. Introduction

The impact of human activities combined with meteorological events [1,2] such as hurricanes and storm surges [3] or sea level rise (SLR) [4–6], affects the sediment fluxes of coastal regions in a significant manner. The presence of vegetation along the shoreline [7,8] contributes in mitigating erosion of the most impacted areas. In fact, such erosion is mainly caused by a high shear stress on the bottom of un-vegetated tidal creeks, often associated with extreme events. The friction of dense vegetation reduces erosion, particularly when the tides are elevated, and the drag created by 2 m-tall marsh plants can be critical in slowing currents [9]. However, the factors mentioned above also impact on the capability of vegetated salt marshes to survive climate change [10–12]. Due to the important role

of coastal wetlands in impacting the sediment transport [9,13] and surface elevation of the marsh [14], the restoration of salt marshes has been of interest since at least 1988 [15]. Primarily, the resilience of salt marshes to climate change is important to develop interventions able to mitigate the impact of extreme, and even catastrophic, events, as well as to understand the evolution of coastal regions [16–18] and to assess their morphological changes. The preservation of the existing marshes and the restoration of the lost ones contribute to limiting land loss in many coastal regions and ensuring the valuable estuarine and coastal ecosystem services [19]. Moreover, the coupling between tidal mudflats and salt marshes affects the marsh morphology [20], as well as the efficiency of tidal channel networks can alleviate aspects such as the drought-induced die-off of salt marshes [21]. This highlights the importance of micro-tidal systems in which salt marshes, mudflats and channel networks can be studied simultaneously.

The Eastern Shore of Maryland, facing the Chesapeake Bay (CB) (Figure 1a), is currently one of the most impacted areas by SLR along the whole East Coast of the United States [22]. SLR also affects coastal processes in many parts of the Bay [23] and the entire region has been subjected to coastal erosion during the last decades. In particular, waves impact marsh boundaries at higher elevation enhancing erosional processes. Extreme events, such as hurricanes, winter storms and strong Nor'easter (Northeaster (commonly contracted Nor'easter) is a northeast wind, particularly a strong wind or gale. Hence, Nor'easter is a cyclonic storm of the east coast of North America, so called because the winds over the coastal area are from the northeast. (adapted from the *Glossary of Meteorology of the American Meteorological Society*: <https://glossary.ametsoc.org/wiki/Northeaster> accessed on 18 March 2021 and https://glossary.ametsoc.org/wiki/Northeast_storm accessed on 18 March 2021)) winds, can cause very large water level excursions (up to some meters). This implies that flood and ebb currents have the strength to magnify the erosion processes caused by ordinary tidal cycles, while, on the other side, it also means that increased wave erosion associated with stronger winds can impact wider areas, since the changing water level causes the waves to break in different zones. In addition, sediment resuspension and transport during tropical storms and Nor'easter could represent a significant term in the sedimentary budget of an estuary [24]. CB is also subjected to subsidence: for an Absolute Sea Level Rise (ASLR) rate of 1.8 mm/yr at late 20th/early 21st century, inferred subsidence rates vary from -4.00 mm/yr at the Chesapeake Bay Bridge Tunnel, VA, to -1.29 mm/yr at Baltimore, MD [25].

Poplar Island, located in the upper-middle CB (Figure 1b), was almost completely lost because of both the erosion and the combination of sea level rise and subsidence [26,27]. The United States Army Corps of Engineers (USACE)–Baltimore District in collaboration with the Maryland Department of Transportation–Maryland Port Administration (MDOT MPA) and in cooperation with Maryland Environmental Service (MES) have established a project focused on restoring the original extent of Poplar Island [26]. The uppermost eastern part of the island is divided into three cells respectively named 1A, 1B and 1C from south to north (Figure 1c). The three cells constitute an overall tidal system with water exchange between adjacent cells. In addition, each cell has its own culvert providing a link with CB. The channel morphology of the cells has been planned studying the channel geometry, tidal dynamics and marsh surface elevation, since marsh morphology depends on different factors such as the relationship between tidal mudflats and salt marshes [20]. Two natural marshes (Hog Island and Chesapeake Bay Environmental Center) were used as a reference for the design of channel morphology in the Poplar Island marshes. Assessing the variation occurred in time, in terms of natural evolution of the initial design of the cell, is important for understanding the actual impact of restoration strategy adopted for mitigating the erosion of shorelines.

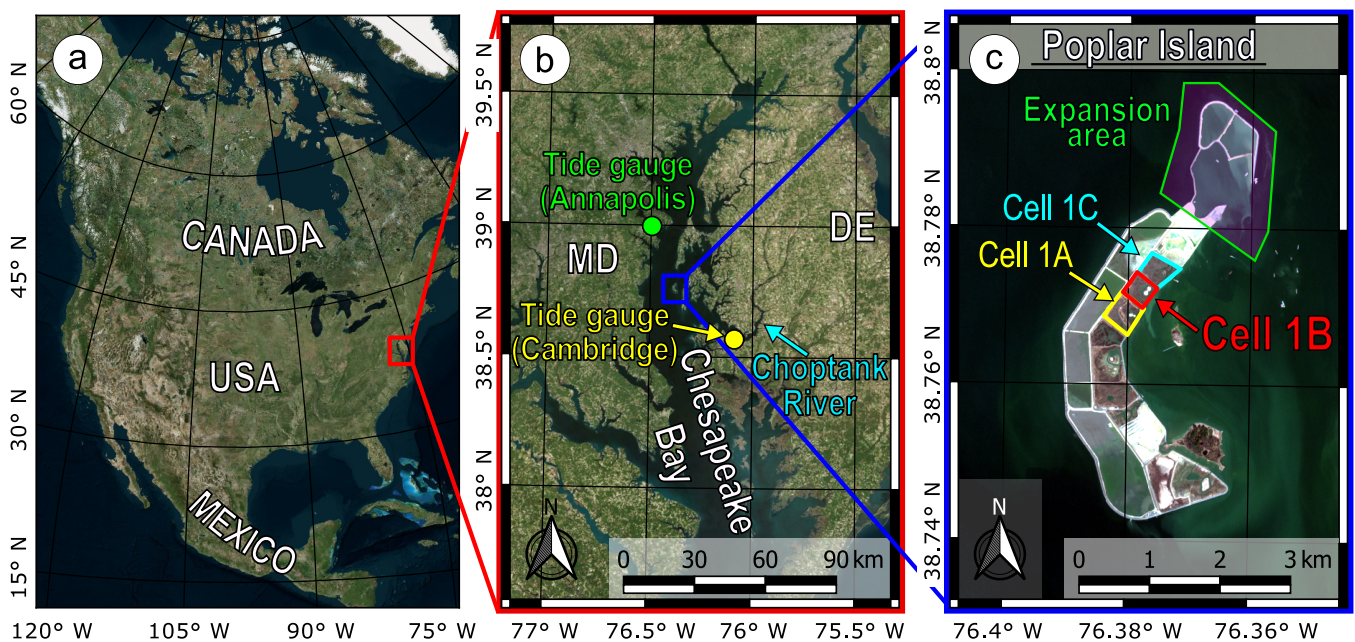


Figure 1. (a): location of Chesapeake Bay along the US East Coast; (b): location of Poplar Island (c): Aerial surveys were performed in Cell 1B. (Satellite imageries from Bing maps and Copernicus Sentinel 2 data [imagery acquired on 12 March 2019]).

Several approaches have been proposed in the literature [28] to evaluate and analyze shoreline changes. The use of satellite images [29] is suitable for large areas and advanced techniques such as a cluster-based segmentation may be applied [30]. However, the accurate detection of small systems requires high resolutions with a Ground Sample Distance (GSD) of a few centimeters. Digital Elevation Models (DEMs) represent primary tools in order to both detecting and characterizing morphology of such systems [31,32]. Different techniques exist for collecting data for DEM generation: (i) direct ground point surveys, (ii) Terrestrial Laser Scanning (TLS), (iii) aerial Light Detection And Ranging (LiDAR) systems and (iv) aerial photogrammetry from Unmanned Aerial Vehicles (UAVs) [33,34]. Direct methods are very time-consuming: (i) requires the survey of each point of interest, whereas (ii) implies post-processing operations to aligning and registering point clouds with the additional task of a data filtering. Aerial LiDAR is similar to (ii), essentially with the difference of a non-terrestrial data acquisition. UAV photogrammetry combines the flexibility of drones in carrying almost every kind of device, in particular cameras, with the Structure-from-Motion (SfM) and Multi-View-Stereo (MVS) approach that allows one to reconstruct the 3D geometry of objects. The density of photogrammetric dense point clouds is comparable to the one of TLS and LiDAR [35–37] and the high spatial resolution is also matched by high model accuracy [38]. For such reasons, UAV photogrammetry has been widely and successfully used in a multitude of applications: coastal environments [39–41], such as the monitoring of dune systems [31,42,43] and beach topography [44–46], river morphology characterization [47], assessment of glacier dynamics [48,49], landslide monitoring [50,51] and also architectural heritage [52,53]. The high level of accuracy achievable with DEMs derived from UAV imageries has been investigated and confirmed [37,54], as well as the reproducibility of the results [55,56].

In this work, we present the use of UAV photogrammetry for assessing the behavior of a micro-tidal system in terms of evolution, with regard to the restored salt marsh, the mudflat and the channel network. In fact, the potential of UAVs for monitoring the morphodynamics of mudflats has been investigated by Jaud et al. [57] in the Seine Estuary, finding out that UAV datasets enable, for instance, multi-scale approaches, but a complete micro-tidal system has not been investigated yet. In particular, the methodology proposed here has been applied focusing on a small cell (Cell 1B, abbreviated as C-1B in

the following) [58], which is located in the middle of the overall tidal system described above and hence C-1B is connected with both Cells 1A and 1C. In fact, C-1B experiences all of the dynamics of CB shorelines. For instance, between 2 March and 10 March 2018 Winter Storm Riley caused a water level range of up to 2 m. This was recorded by tide gauges in Cambridge (Figure 2) along the Choptank River and in Annapolis. Both the tide gauges are about 30 km away from Poplar Island. Considering that the total (maximum) predicted (Tide predictions have been retrieved from NOAA (National Oceanic and Atmospheric Administration) at <https://tidesandcurrents.noaa.gov> accessed on 3 June 2019. Predictions reported here does not account for local meteorological effects.) tidal range during the winter storm (without storm effects) is approximately 0.7 m, this was a typical Nor'easter. In order to evaluate the evolution of the cell under SLR and meteorological events, a monitoring over time has therefore been started.

The aim of the proposed study is to apply a simple and flexible survey procedure to help and improve tidal system monitoring, also for providing basis for high-resolution numerical modeling of small tidal systems, exploring the potential of UAVs in this field. Moreover, the study site selected for the methodology development is one of the first worldwide restoration project where an interdisciplinary marsh design has been tested. Due to the small size of both the restoration project and the features of interest, traditional satellite remote sensing (e.g., Landsat 8, Sentinel 2 imagery) does not have a sufficient ground resolution and an innovative monitoring method is needed for tracking geomorphological and ecological changes on a short time scale and with a quick time frame. Originality consists of applying this approach to a small cell (micro-tidal system) in order to assess the evolution over time investigating the feasibility of the overall procedure and evaluating the actual level of accuracy attainable.

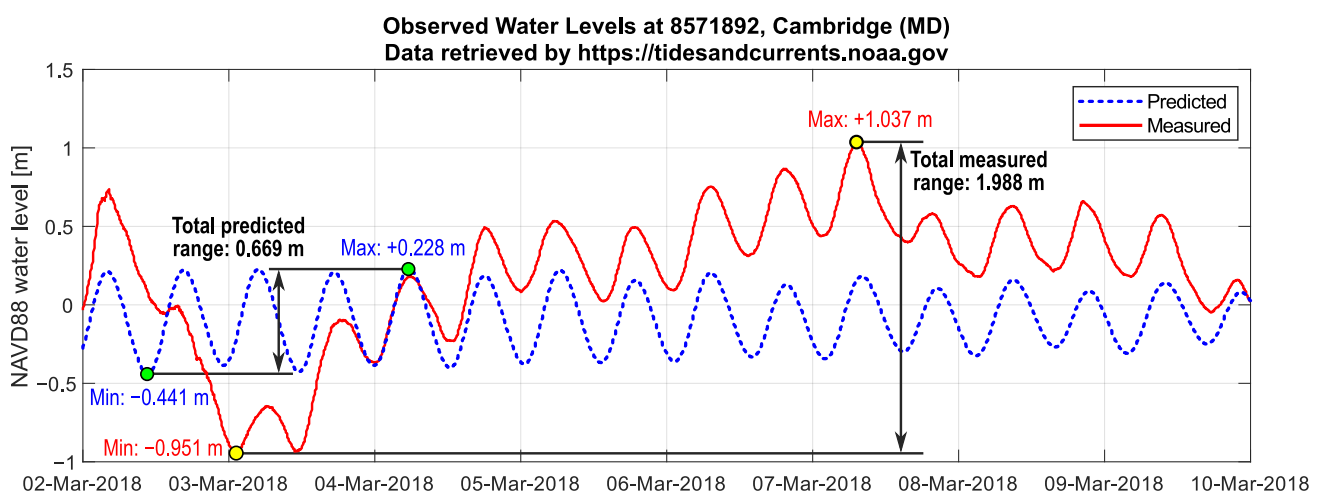


Figure 2. Water level excursion during the effects of winter storm Riley in March 2018 at Cambridge (MD). The vertical datum is the same as for all the aerial surveys (NAVD 88). Measured values refer to those verified by NOAA.

2. Materials and Methods

In this section, we present the survey methodology (Figure 3) based on UAV photogrammetry together with ground GNSS RTK survey that was adopted for the reconstruction and characterization of the 3D geometry of C-1B. The morphology of the different parts of the cell (illustrated in Figure 4) was directly assessed through a comparison over time to identify possible erosion processes that are in progress. In order to achieve this result, we tested a methodological approach to collect geospatial information about the cell morphology: acquiring aerial imagery from UAV to evaluate the distribution of the vegetation and to generate Digital Terrain Models (DTMs) of the emerged areas, performing a GNSS RTK survey to integrate missing data in submerged channel areas and to collect the coordinates of Ground Control Points (GCPs). The procedures presented below can hence be replicated in practice in any similar environment all over the world.

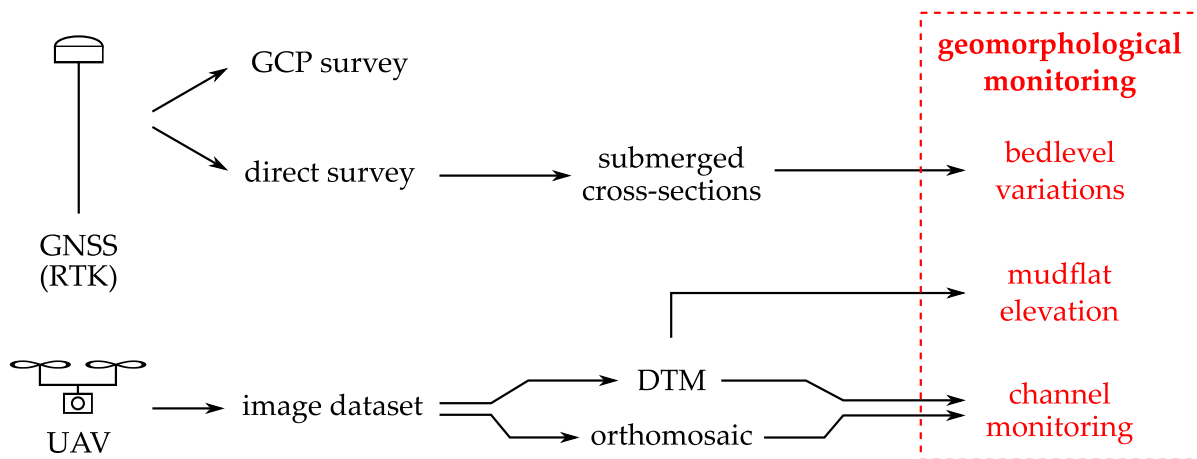


Figure 3. Summary of the methodological approach proposed for tidal system monitoring.

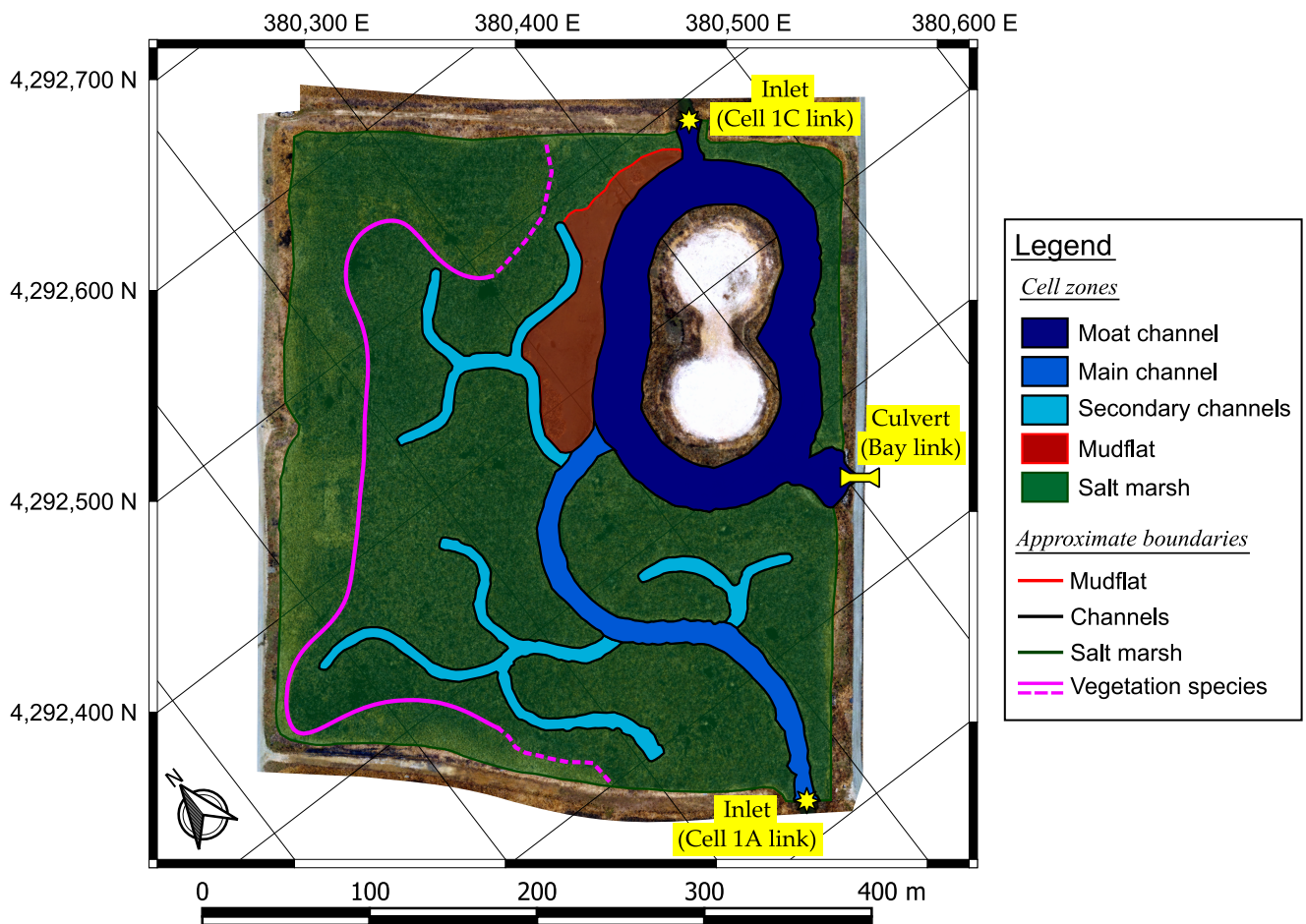


Figure 4. Description of the parts of Cell 1B. (Background is the 2019 orthomosaic).

2.1. Image Acquisition and Related In-Situ Operations

Cell mapping with a centimeter-level ground resolution can be performed using a camera mounted on a small UAV and flying at an appropriate altitude. In this methodological research, we used a DJI Phantom 3 Professional (DJI-P3P) multicopter equipped with the DJI FC300X camera for image acquisitions. In fact, this is a versatile, lightweight and easy-to-use drone. Aircraft and camera specifications [59] are reported in Table 1. The theo-

retical Ground Sample Distance (GSD), that represents the pixel size on the ground, can be computed as:

$$GSD = \text{pixel size} \cdot \frac{\text{flight altitude}}{\text{focal length}} \quad (1)$$

and hence depends on the actual flight altitude of the UAV. In order to obtain a GSD of ≈ 2 cm, we planned image acquisition at a 40 m altitude: in this way, the theoretical GSD is 1.8 cm. The first aerial survey was performed in April 2018 and a total amount of three flight missions were planned and executed for the survey of the entire extent of the cell.

A second survey was also carried out one year later (in April 2019) using the same DJI-P3P drone. In this case, four different flight missions were necessary for the mapping of the cell, due to the need for limiting the flight time to about 10–12 min. Finally, a third aerial, the last for this methodological investigation, survey was also performed in November 2019 with the vegetation close to the end of its seasonal cycle. Photo density was found to be sufficient (with more than 9 images per ground point) to ensure a high number of reprojections of each ground point on the acquired images for each image dataset we processed. Flight plan parameters are shown in Table 2. With regard to water levels (tide conditions), the survey in April 2018 was performed in high tide (approximate water level of about +0.10 to +0.20 m NAVD 88), while the April 2019 and November 2019 in mid-low tide (approximate water level of about -0.10 to 0.00 m NAVD 88).

Table 1. Aircraft and camera specifications.

Aircraft Specifications	
Type	DJI Phantom 3 Professional
Take off weight	1280 g
Max flight speed	16 m/s
Max flight time	≈ 23 min
Horizontal hovering accuracy	$\pm 0.3 \div 1.5$ m
Vertical hovering accuracy	$\pm 0.1 \div 0.5$ m
Camera Specifications	
Name	DJI FC300X
Type	RGB
Focal length	3.6 mm
35 mm equiv. focal length	20 mm
Image resolution	4000×3000
Field of view	84°
GSD at 40 m altitude	≈ 1.8 cm

In order to perform a model georeferencing with a final centimeter-level accuracy, a set of GCPs and Check Points (CPs) were deployed every time. Each GCP/CP consisted of a target of about $60 \text{ cm} \times 60 \text{ cm}$, clearly visible on the acquired images. Coordinates of the GCPs were collected using two Topcon HiPer V geodetic receivers in Real-Time Kinematic (RTK) mode. The base station was set up on a benchmark at the edge of the cell (see Figure 5), while the rover was used to record the coordinates of the center of each target with a 30-s Stop-and-Go. Figure 5 illustrates the location of GCPs and CPs for the survey repetitions of April 2018 and April 2019. In addition to GCPs and CPs, non-signalized Validation Points (VPs) were also surveyed in RTK mode for an accuracy assessment of the DTMs. All the coordinates were recorded in NAD 83(2011) reference system, while ellipsoidal heights were converted into orthometric elevations referred to the NAVD 88 vertical datum by applying the GEOID12B separation model. It is worth noting that the RTK mode used in this work can be replaced with a Network RTK (NRTK) in most situations. However, RTK mode can be easily used in any kind of environment, simply monumenting a local base benchmark.

Table 2. Flight plan specifications.

Flight Plan Specifications	
Number of missions	3–4
Altitude	40 m AGL
Longitudinal overlap	80%
Side overlap	60%
Speed of aircraft	ca. 5 m/s

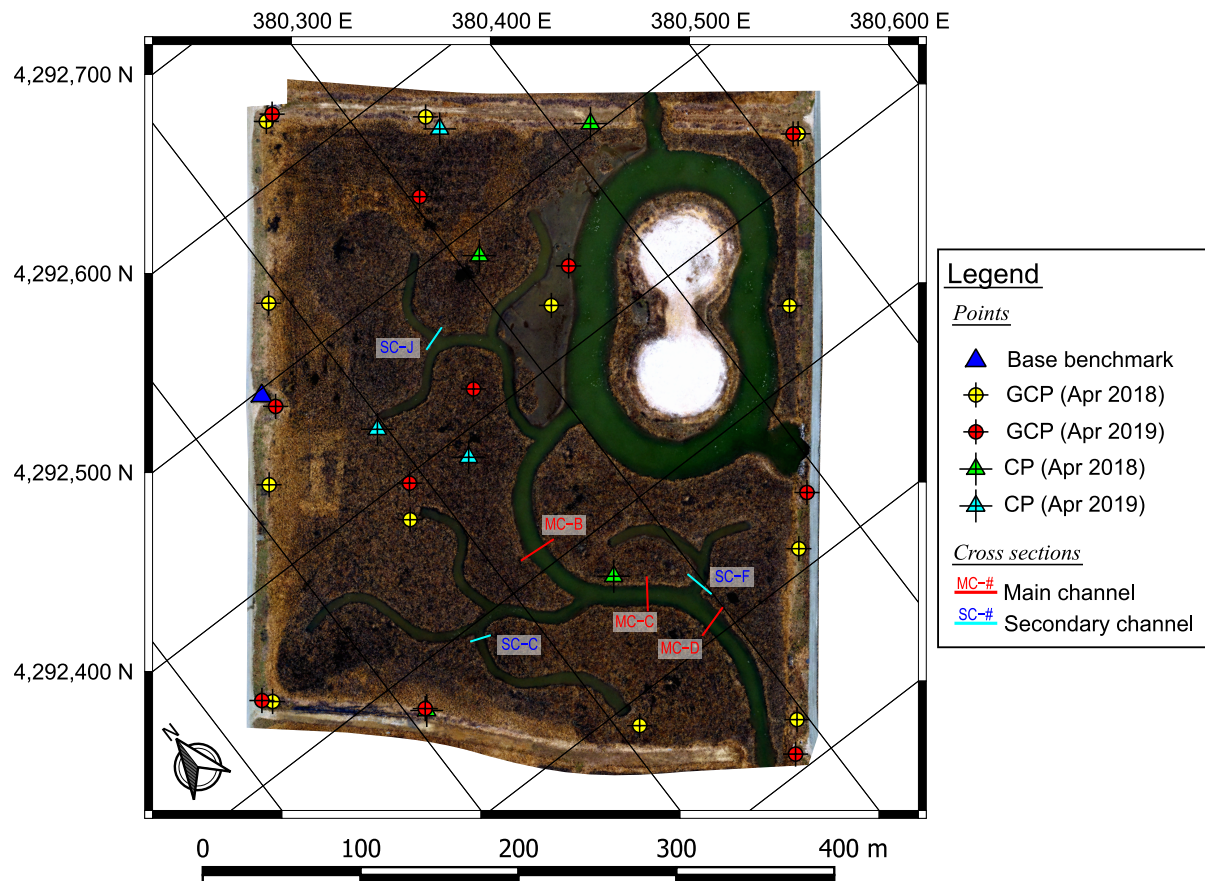


Figure 5. Ground Control Points (GCPs) and Check Points (CPs) used for aerial surveys in April 2018 and April 2019. The location of monitored cross-sections on main and secondary channels is also reported. (Background is the 2019 orthomosaic).

2.2. Photogrammetric Reconstruction

UAV-acquired images were used to reconstruct the three-dimensional geometry of the cell by using an SfM-MVS approach. The image datasets acquired during aerial flights (see Section 2.1) were processed in Agisoft PhotoScan/Metashape Professional software. The overall process, from the stage of the acquisition planning (desired GSD, flight altitude and number of missions) to the generation of final products of the photogrammetric workflow, is depicted in Figure 6. The reconstruction of the geometry using SfM-MVS essentially consists in (i) detecting features on the images and describing them using, for instance, scale invariant feature transform (SIFT), then (ii) matching the features across the different images looking for correspondences and filtering out outliers and finally (iii) performing a Bundle Block Adjustment (BBA), also taking into account the camera model estimation (interior orientation parameters through a self-calibration).

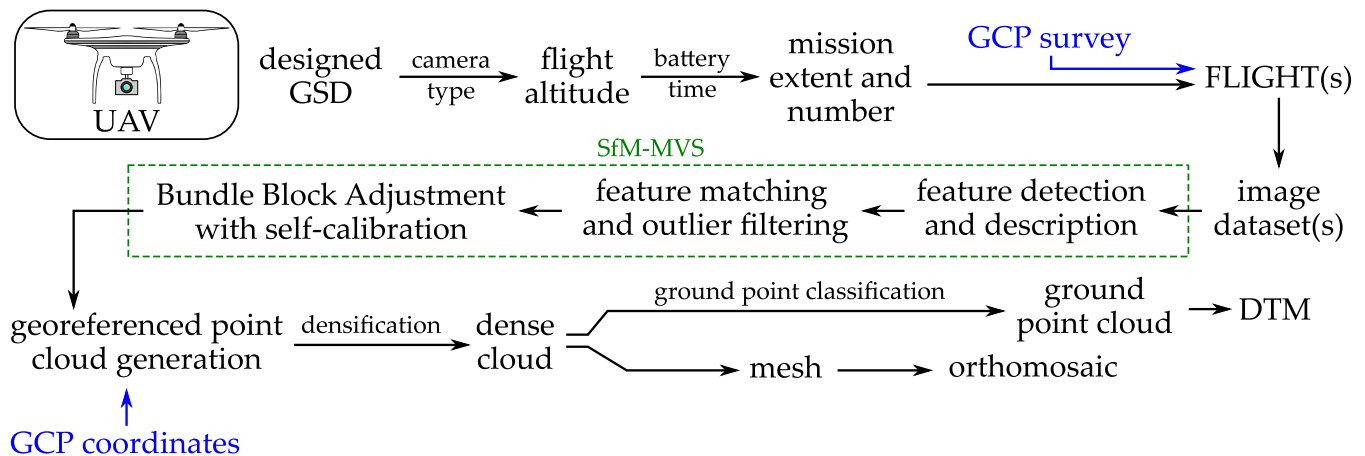


Figure 6. UAV photogrammetry process.

In order to increase the accuracy of the sparse point cloud made up of all the tie points detected on the images and successfully matched, those points with a low reprojection accuracy (threshold used in Agisoft PhotoScan/Metashape: 0.3) or a high reconstruction uncertainty (threshold used in Agisoft PhotoScan/Metashape: 10) were removed prior to continuing the data processing. In these initial stages, the GCPs were introduced (i.e., specified on every image and provided with their own surveyed coordinates). In this way, the photogrammetric model was georeferenced. Finally, non linearities in camera modeling were considered through a global optimization of the interior orientation parameters: focal length f , principal point offset c_x, c_y , affinity and non-orthogonality (skew) coefficients b_1, b_2 , radial distortion coefficients $k_1 - k_3$, tangential distortion coefficients $p_1 - p_4$ [60]. Processing parameters used in the software are reported in Table 3.

Table 3. Processing parameters.

Alignment	
Camera model	Normal
Accuracy	High
Key point limit	200,000
Tie point limit	20,000
Optimization	$f, c_x, c_y, b_1, b_2, k_1 - k_3, p_1 - p_4$
Depth Maps and Dense Point Cloud	
Quality	High
Depth filtering	Aggressive

The assessment of the actual modeling accuracy was carried out by using the CP dataset: the comparison between model-derived coordinates and surveyed coordinates provided an indicator of the overall level of accuracy of the 3D model. The residuals computed for the aerial survey performed in April 2018, for both GCPs and CPs, are shown in Table 4. Values obtained for the survey in April 2019 and November 2019 were found to be similar.

Dense point clouds were reconstructed within the same software. In this work, dense clouds were made up of 55,000,000 to 170,000,000 points for the overall extent of the cell, leading to an average point density spacing from a little less than 400 points/m² to almost 1200 points/m². A further procedure to filtering out the vegetation was also applied using a built-in function of Agisoft PhotoScan/Metashape. This method splits the entire model into a grid of cells with a user-defined size, then assumes that the lowest point within each cell (5 × 5 m) belongs to the ground and finally classifies all the remaining points on the basis

of angle and distance thresholds [60]. From the classified ground points, a georeferenced Digital Terrain Model (DTM) was generated and exported. Similarly, a centimeter-level orthomosaic was also generated and exported from each photogrammetric model.

Table 4. Residuals for Ground Control Points and Check Points (April 2018).

	Ground Control Points			
	East	North	Elevation	3D
Average [m]	−0.001	0.000	+0.003	0.021
Min [m]	−0.024	−0.029	−0.017	0.012
Max [m]	+0.022	+0.021	+0.025	0.045
RMSE [m]	0.013	0.014	0.013	0.023
	Check Points			
	East	North	Elevation	3D
Average [m]	−0.005	−0.006	+0.004	0.019
Min [m]	−0.027	−0.040	−0.001	0.001
Max [m]	+0.013	+0.012	+0.009	0.049
RMSE [m]	0.015	0.021	0.005	0.026

In addition, a VP-based validation of the DTM was also performed prior to analyzing morphology changes. Despite the application of a slope detection algorithm to classify ground points in Agisoft PhotoScan/Metashape, the DTM did not reach a centimeter-level accuracy in vegetated regions (i.e., salt marsh). Figure 7 shows the location of VPs and the difference between the GNSS elevation and the April 2019 DTM elevation ($H_{GNSS} - H_{DTM}$). The results, divided per region (i.e., salt marsh, mudflat and channel edges) are reported in Table 5. The vertical error ranged from a few centimeters to a maximum of about 40 cm into the salt marsh. This represents a common and expected issue in marshes with dense vegetation [61–63]. In un-vegetated zones the differences were found to be lower, with RMSE values comparable to the expected accuracy of the DTM. Similar values were found for the other aerial surveys in this work.

Table 5. Validation results in the different regions of the tidal system.

Region	Max Difference [m]	Min Difference [m]	Average [m]	RMSE [m]
Salt Marsh (vegetated)	−0.027	−0.394	−0.181	0.199
Mudflat (un-vegetated)	+0.004	−0.027	−0.011	0.015
Channel Edges (un-vegetated)	+0.021	−0.025	+0.003	0.015

Hence, a centimeter-level vertical accuracy was obtained in un-vegetated regions (i.e., channel edges and mudflat). Figure 8 illustrates the location of a wider dataset of VPs on the mudflat and the distribution of elevation differences computed again as $H_{GNSS} - H_{DTM}$ for each VP. The mean value of −0.8 cm and the standard deviation of 2 cm confirmed the level of accuracy mentioned above. Also, the standard deviation is still comparable with the 3D Root Mean Square Error (RMSE) of GCPs and CPs (see Table 4). Due to the high uncertainty of the DTM in vegetated regions, in this work we did not process elevation data of the salt marsh platform to track geomorphological changes.

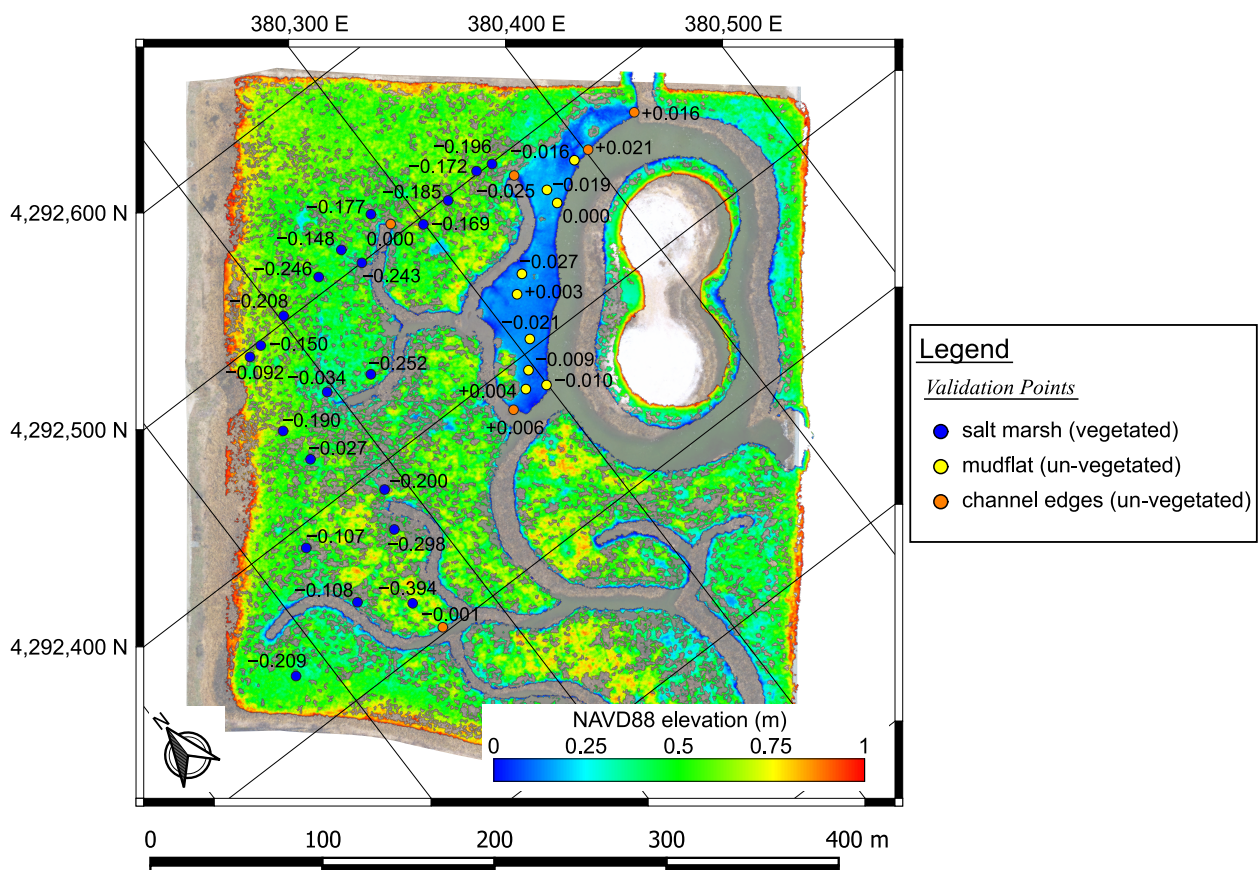


Figure 7. Spatial distribution of Validation Points (VPs) used for the assessment of DTM accuracy. Elevation differences reported were computed as $H_{GNSS} - H_{DTM}$. Vegetated regions show a poorer accuracy due to the presence of vegetation. (Background is the April 2019 elevation).

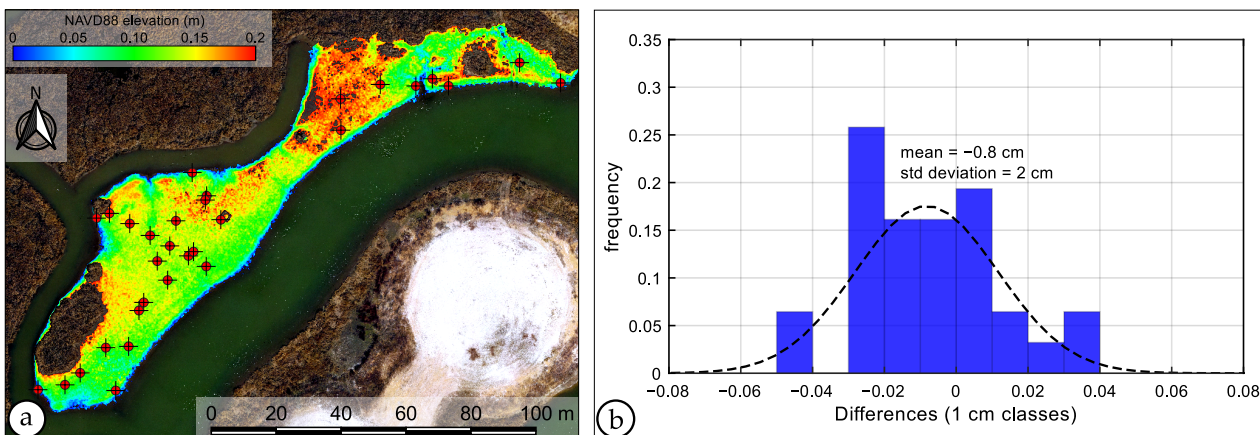


Figure 8. (a): spatial distribution of the mudflat points used for the validation of the DTM (colored background provides the mudflat elevation within the range from 0 to +20 cm); (b): frequency distribution of discrepancy values between GNSS elevation of validation points on the mudflat and the corresponding elevation extracted from the DTM computed as $H_{GNSS} - H_{DTM}$.

2.3. Initial as-Built Dataset

Data collected by aerial flight missions and GNSS RTK was compared to the initial status of C-1B (in 2012) provided by the MES. The initial profile of a total of six cross-sections (see Figure 5) was hence reconstructed using the elevation data. Three cross-sections were selected along a main channel and the remaining were located on the secondary channels. Also, an as-built point dataset was used to evaluate elevation variations on the mudflat

using a discrete (point-by-point) approach. Vegetation planting design was also provided to us.

2.4. Vegetation Boundary for Evaluating Channel Width

The high-resolution orthomosaic generated from UAV-acquired images [41,64] and the GNSS survey data were then used for evaluating the morphology of the channels. In this work, we evaluated the channel width for each monitored cross-section through two different approaches. Since the possibility to assess the channel width from a DTM depends strongly on the water level (tide conditions) at the time of each survey, here we propose an alternative method based on vegetation boundary to assess lateral variations as first approach.

The first aerial survey was performed in high tide conditions (April 2018), with a water level $WL_{NAVD\ 88} \geq 5\text{--}10\text{ cm}$ and hence with the channel banks almost completely submerged. This situation should be avoided in general. However, in practice, the possibility to acquire aerial images is often too much related to wind speed in the middle of the bay, thus waiting for low tide could be almost not feasible in most situations. This led us to consider the use of vegetation boundary on the salt marsh to evaluate lateral erosion along the scarps as well as the channel width. In fact, due to the vegetation that is present on the salt marsh platform and that is suddenly interrupted whenever these scarps are present, the erosion can be recognizable with almost any water level. It is also worth noting that the mapping using this approach was repeated twice in similar conditions of the seasonal growth of the vegetation (in April 2018 and April 2019, respectively). This ensured the best level of repeatability of the mapping operations based on UAV orthomosaics for channel width evaluation. A third repetition was finally conducted on November 2019 data.

The detection of the erosion scarp mentioned above consisted in a manual mapping carried out on the orthomosaics with a GSD of about 2 cm. Operator error magnitude (σ_{op}) can be estimated as a few GSDs (up to $\sigma_{op} = 10\text{ cm}$) on each channel bank. Channel width error is hence $\sigma_w = \sqrt{2 \cdot \sigma_{op}} \approx 0.15\text{ m}$. Such a value appears to be quite high, but it is worth noting that vegetation loss is often at a level of clods, since the roots entrap a wide portion of soil. For this reason, we did not consider as significant width variations less than 2%. This threshold corresponds to a variation of $\sigma_w = 0.15\text{ m}$ over a total width of $w = 7.5\text{ m}$. Then, we computed the variation rate per year twice for the period 2018–2019 as:

$$\Delta w_1 = \frac{w_{Apr.\ 2019} - w_{Apr.\ 2018}}{w_{Apr.\ 2018}}, \quad \Delta w_2 = \frac{w_{Nov.\ 2019} - w_{Apr.\ 2018}}{w_{Apr.\ 2018}} \cdot \frac{12}{19} \quad (2)$$

where the factor $\frac{12}{19}$ takes into account the actual number of months. Also, we computed the average $\overline{\Delta w} = \frac{\Delta w_1 + \Delta w_2}{2}$.

2.5. GNSS RTK Survey: Cross-Section Profiles and Channel Width

In order to reconstruct the profile of cross-sections and integrate the aerial surveys, a direct GNSS RTK survey can be carried out. This method was used for surveying cross-section points located within the channels. This made it possible to acquire additional information in submerged regions to assess (i) the evolution of the bedlevel elevation and (ii) the shape of lateral slopes for further analyzing the effect of real shear stresses, making available, at the same time, (iii) a second approach to evaluate a more accurate channel width. Due to the high time consumption of this task, however, the GNSS RTK survey can be performed with a longer time frame (1–2 years). In general, the temporal resolution depends on the hydro-dynamic conditions and marsh type of the monitored site. The availability of as-built data allowed us to reconstruct the initial shape of the profiles for a comparison over time. The georeferencing of all of the surveys within the same NAD 83(2011) horizontal datum is a crucial aspect to ensure a consistent comparison of the cross-sections with respect to each channel axis, without any significant lateral offset. For the same reason, elevations were referred to the NAVD 88 vertical datum in this work.

In this research, we assumed a reference elevation at a water level $WL_{NAVD88} = 0$ m. In fact, this elevation represents a good indicator for channel width in C-1B (see Figure 9) with respect to the predicted tide levels reported in Figure 2.

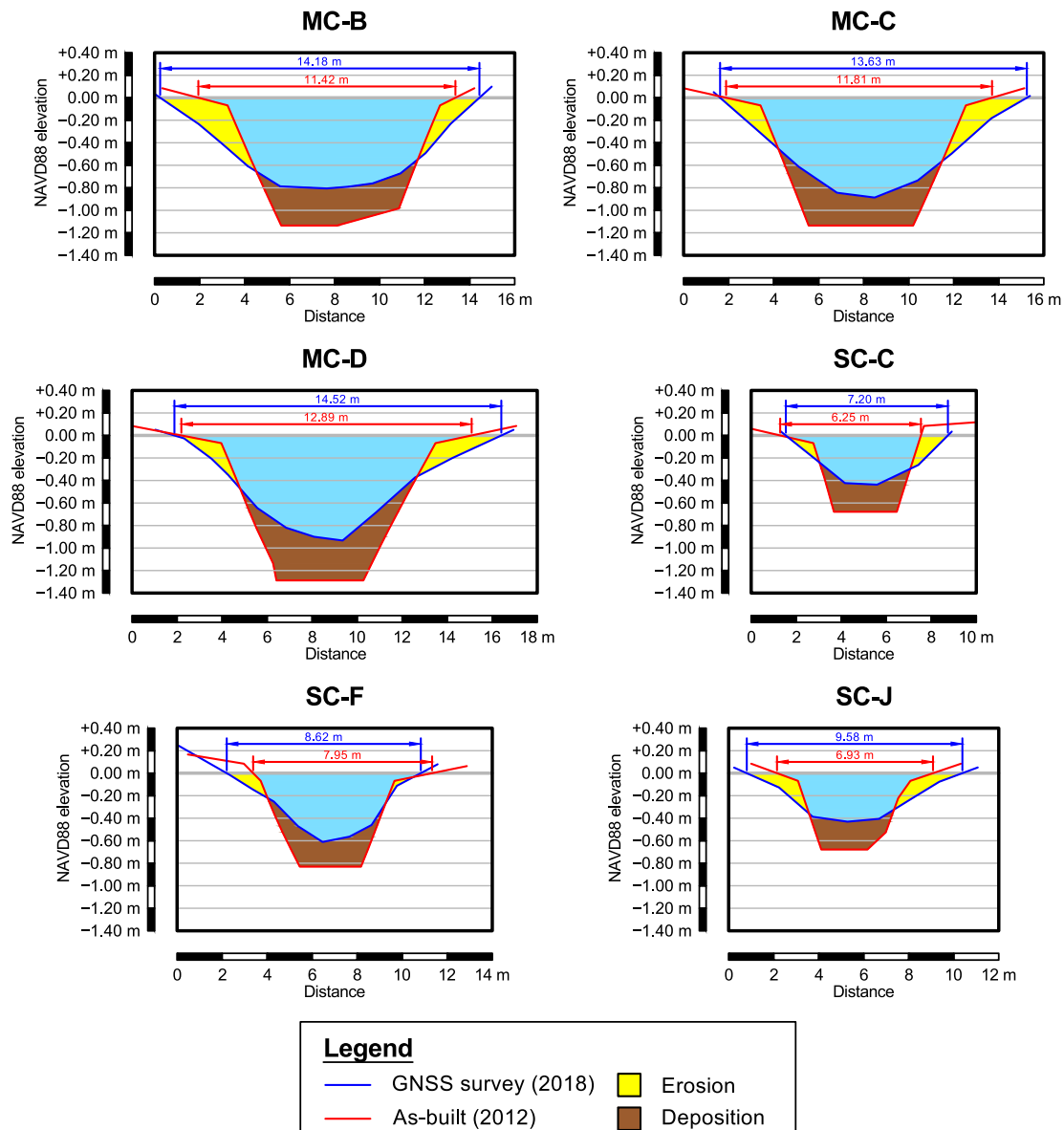


Figure 9. Profiles of the cross-sections shown in Table 7, surveyed in 2018 (GNSS) and 2012 (as-built).

2.6. Elevation Variations on the Mudflat

In addition to mapping channel edges and estimating channel widths, an assessment of the elevation variations on the mudflat can be carried out. This region experiences sedimentation and erosion whose effects are not reduced by the vegetation. In order to compare the morphology of the cell with its initial one (in 2012), the elevations extracted from the DTM were considered. In particular, we performed an analysis using the point dataset described in Section 2.3. An average 2018–2019 elevation (\bar{H}) and its variation from the time of as-built data (i.e., 2012) was computed. This assumption is feasible for our purpose of evaluating the elevation change over ca. 6 years due to the centimeter-level accuracy of DTMs and sedimentation/erosion rates on the mudflat not exceeding this threshold over a single year and also allowed us to exclude possible outliers from the comparison.

3. Results

3.1. Vegetation Boundary for Evaluating Channel Width

As mentioned in Section 2.4, channel width was estimated for six cross-sections. Channel width estimates based on the vegetation boundary are reported in Table 6. Also, the variation rate Δw per year is reported together with the width estimates. The location of each cross-section (with abbreviations) is shown in Figure 5.

Table 6. Channel width: vegetation boundary (I approach).

Cross-Section	Orthomosaic (Apr. 2018)	Orthomosaic (Apr. 2019)	Orthomosaic (Nov. 2019)	Δw_1 (per Year)	Δw_2 (per Year)	$\overline{\Delta w}$ (per Year)
MC-B	14.9 m	15.3 m	15.8 m	+2.7 %	+3.8 %	+3.2 %
MC-C	14.6 m	14.6 m	14.3 m	< ± 2 %	< ± 2 %	< ± 2 %
MC-D	15.4 m	15.5 m	15.6 m	< ± 2 %	< ± 2 %	< ± 2 %
SC-C	7.8 m	8.3 m	9.2 m	+6.4 %	+11.3 %	+8.9 %
SC-F	9.5 m	9.5 m	9.4 m	< ± 2 %	< ± 2 %	< ± 2 %
SC-J	10.4 m	10.4 m	10.7 m	< ± 2 %	< ± 2 %	< ± 2 %

With regard to the main channel, MC-B seems to show a moderate enlargement. On the contrary, MC-C and MC-D can be assumed as stable considering the uncertainty of channel width using the vegetation boundary. The secondary channel cross-sections, instead, present different situations. SC-C shows a moderate enlargement in 1-year period, significantly extending itself from April 2019 to November 2019. SC-J and SC-F did not show significant variations. Both MC-B and SC-C enlargements were due to a loss of some clods of muddy soil with vegetation on the right side of the respective cross-section. This was confirmed by a visual inspection of the orthomosaics.

3.2. GNSS RTK Survey: Cross-Section Profiles and Channel Width

Channel width was also estimated in correspondence of a water level assumed as a reference, as previously mentioned in Section 2.5. Table 7 reports the results we obtained with this approach. It is worth noting that the values reported in Tables 6 and 7 cannot be compared since the approach we adopted was different (i.e., vegetation boundary vs. elevation).

Table 7. Channel width: GNSS RTK survey (II approach).

Cross-Section	As-Built (2012)	Survey (2018)	Variation Rate
MC-B	11.42 m	14.18 m	$\approx +4\%$ /year
MC-C	11.81 m	13.63 m	$\approx +3\%$ /year
MC-D	12.89 m	14.52 m	$\approx +2\%$ /year
SC-C	6.25 m	7.20 m	$\approx +3\%$ /year
SC-F	7.95 m	8.62 m	$\approx +1\%$ /year
SC-J	6.93 m	9.58 m	$\approx +6\%$ /year

We can note that all of the cross-sections are wider than the time they were built. On average, the variation rate is up to $\approx +6\%$ per year. Looking at the profiles (see Figure 9) directly surveyed in GNSS RTK mode and compared to the initial (and almost trapezoidal) shape derived from the as built data (2012), we can note that the shape is deeply changed, with a rounding also due to the properties of the fine and cohesive sediment which the cell is made up of. Both MC and SC cross-sections highlighted a lateral erosion on left and right sides as well as a deposition on the channel bed. In particular, the profiles of the MC cross-sections (MC-B, MC-C and MC-D) showed a deposition up to ≈ 40 cm in proximity of the center of the channel. Similarly, a value of about 20 cm has been generally detected for the secondary channels. Lateral erosion trends have been found to be more spatially variable across the monitored cross-sections. Most of the variations we found took place at elevations that are regularly exposed to the air and submerged during tide cycles (intertidal). Additionally, due to the low velocities in the channelized

area, the cross-sections showed deposition at the bottom of the tidal creeks. An important role is might played by the sediment dynamics which is locally removed from lateral banks and deposited right at the center of the channel.

3.3. Elevation Variations on the Mudflat

The elevation variation on the mudflat, computed using \bar{H} as reported in Section 2.6, is shown in Figure 10. Points presenting elevation losses are located close to the channel edges. This further confirms the presence of lateral erosion along the channels since the construction of C-1B (in 2012). The average elevation loss is 4.5 cm for the moat channel and 3.6 cm for the secondary channel. Points located near the vegetation on the mudflat showed a significant elevation increase ($\approx +7$ cm on average). This is due to sediment trapping and organic matter production [65].

Conversely, the inner region of the mudflat is characterized by lower elevation changes and seems to be essentially stable in the last period. However, the mudflat area shows local signs of erosion which might highlight elevated variability in all the area. Rates of elevation change detected in this region (+0.5 cm on average) have the same magnitude of the model uncertainties that were evaluated through the quality assessment of photogrammetric model and DTM (i.e., using CPs and VPs). Such variations cannot be considered as significant.

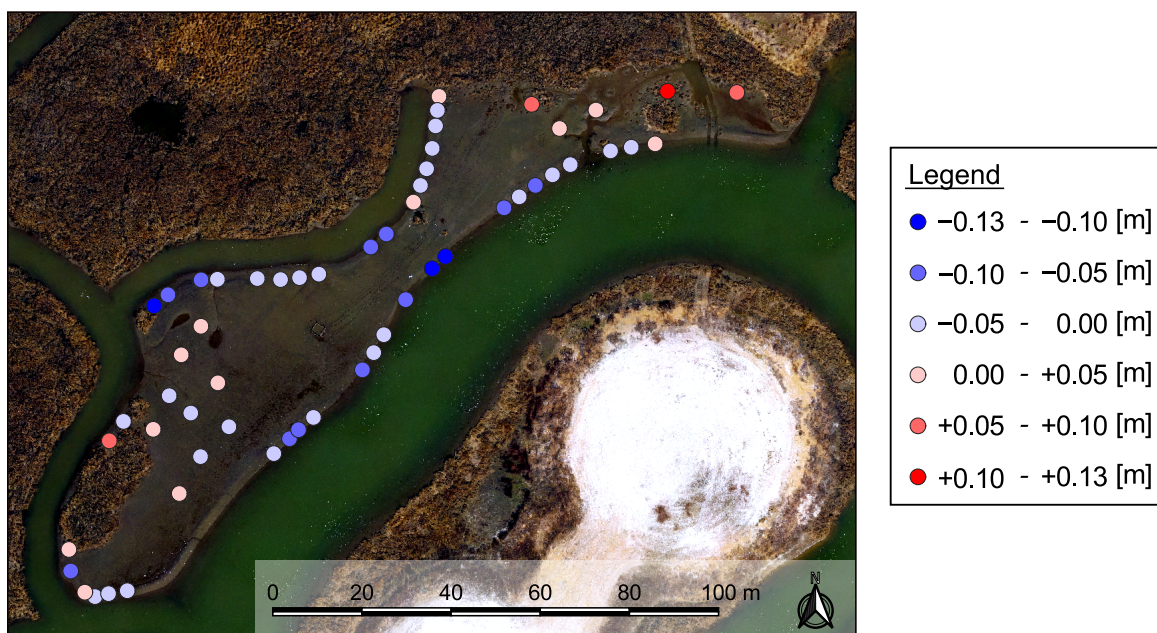


Figure 10. Mudflat elevation variations.

4. Discussion

The results of the methodology adopted in this first case study on restored salt marshes located in a micro-tidal system allowed us to reconstruct the three-dimensional geometry of the cell (i.e., C-1B) with a centimeter-level ground resolution with the possibility of monitoring geomorphological variations with respect to previous conditions. The quality assessment of photogrammetric models is performed with CPs for the validation and confirmed the centimeter-level accuracy of the 3D reconstruction obtained in this work. The subsequent introduction of VPs (i.e., non-signalized points) is useful to evaluate the quality of the DTM and highlighted that only un-vegetated regions reached a centimeter-level accurate elevation in this research, since the vegetation in the salt marsh was not adequately filtered by ground point classification algorithms. This is an expected issue whenever the vegetation is very dense. However, the overall survey accuracy of about 2 cm, due to both the GNSS survey in RTK mode and the GSD of the aerial datasets, allows one to

evaluate the progress of channel morphodynamics and vegetation variations. Difficulties related to the presence of the vegetation could be overcome using, for instance, a different approach based on UAV-LiDAR systems to obtain vegetation characteristics [66]. In fact, a new algorithm has been applied to high-resolution UAV-based LiDAR point clouds for estimating ground elevation, vegetation height and vegetation density in coastal salt marshes, without the necessity of additional datasets (such as direct ground GNSS surveys). This method proved to produce maps of ground elevation and vegetation characteristics (of *Spartina alterniflora*) with a resolution of $40 \times 40 \text{ cm}^2$ [67].

In general, two different approaches can be adopted for evaluating channel width variations in correspondence of selected cross-sections. In this work, we evaluated the channel width for a total of six cross-sections using (i) the high-resolution orthomosaics through an image-based mapping of vegetation boundary and (ii) the direct survey of the entire profile with a GNSS RTK approach. Width estimates based on GNSS RTK have been also compared to the as-built survey of the cell (2012) since both the elevation data have been referred to the NAVD 88 vertical datum for a consistent comparison. Using vegetation boundary for estimating channel width and monitoring lateral erosion trends proved to be a quick approach characterized by a low level of accuracy ($\sigma_w \approx 0.15 \text{ m}$). However, the land loss due to the entrapping of *Spartina alterniflora* roots is often at a level of clods, and hence recognizable. Moreover, this approach can be also used in high tide conditions if the vegetation is not submerged. In order to integrate aerial surveys with data collected in the submerged regions of the channels, cross-sections can be also surveyed with GNSS RTK to reconstruct the corresponding profiles. This method is similar to the technique commonly used to integrate topography and bathymetry data, in which the vertical reference [68] is still crucial to ensure an accurate and consistent reconstruction of the overall morphology. However, this is a time-consuming task and its repetition can be performed less frequently than the mapping based on orthomosaics. Here, the comparison of cross-section profiles with as-built ones highlighted a deposition of sediments on the bed of both main and secondary channels. A general increase of about 20 cm has been found in the middle of the channels, with a maximum up to $\approx 40 \text{ cm}$. At the same time, the additional information provided by GNSS data has shown how the deposition on the bed of the channels mentioned above is also matched by a lateral erosion of the submerged slopes. This change of shape is correlated with the real shear stresses caused by ordinary tidal cycles [69]. In addition, the pronounced curvature of the channels can enhance the impact of the incoming and outgoing fluxes on certain channel banks. The channel width trends found are essentially consistent with orthomosaic-based mapping carried out on a 1-year reference period.

An elevation assessment has been also performed for the mudflat, with a focus on the recent stabilization. Its innermost region has been found to be stable and detected elevation variations were within the range of modeling errors. Conversely, points assessed on the edges of the mudflat, close to the channel edges, lost elevation. This fact further confirms the general lateral erosion highlighted by the monitoring over time performed in correspondence of the cross-sections. A moderate elevation increase was found near the vegetation on the mudflat. This marsh platform accretion represents the response to SLR [18]. For tidal flats it is important to highlight that the presence of water ponds and/or water layers can interfere with the DTM retrieval. Flying when the water level is increasing can help to mitigate and prevent this issue, leaving time to small water ponds to disappear if possible. Conversely, flying when the water level is decreasing gives the possibility to survey more emerged areas within the channels and on the channel banks. Hence, the optimal solution for performing UAV surveys should be carefully evaluated on the basis of which kind of data has to be collected.

Even if we still have a partial understanding of the forces driving tidal marsh resilience, the methodological imprint presented in this study, along with its preliminary results obtained in a micro-tidal system on Poplar Island (USA), establishes that channel design and vegetation growth are key processes for salt marsh restoration and their assessment over

time is crucial. Belliard et al. [70] state that the impacts of vegetation on sediment deposition might be enough for marshes to withstand low amounts of SLR, however, numerical models forecast wide amount of marsh loss in tidal system with moderate to high levels of SLR (>10 mm/yr) and hence restoration interventions should be deeply investigated with a short time frame to establish the most efficient way to restore salt marshes.

Therefore, it is important that numerical modeling, tidal system monitoring and restoration actions improve rapidly enough to suggest actions to counteract the most severe SLR projections. Fleri et al. [27] showed that vegetation characteristics and channel stability are integrally linked.

Recently, restoration projects by ecological engineers in Black Water National Refuge in Maryland (USA) are focusing on channel digging in natural marshes as a solution for dredging swamped area under erosion. Those recent interventions show the crucial role of channels network, and additionally, demonstrate how excavating new channels as an extension of a natural tidal creek will connect the flooded parts of the marsh to the bay draining the entrained water.

5. Conclusions

This work highlights how the use of UAV+SfM-MVS and GNSS RTK surveying allows the monitoring over time of a micro-tidal system. The very high spatial resolution of orthomosaics and DTMs, especially if further combined with a high temporal resolution in terms of small-time lapse between survey repetitions, enables the assessment of cell morphology with a centimeter-level ground resolution and accuracy on tidal flats, while issues were encountered for salt marshes due to the presence of vegetation. Channel width, that is an indicator of lateral erosion, can be assessed with an uncertainty of ≈ 0.15 m from orthomosaics, enabling a quick mapping at almost any water level (tide conditions). More accurate data can be collected through a GNSS RTK survey of channels, but this task is very time-consuming and hence can be used less frequently.

Because of the low operative costs in using UAVs, survey repetitions can be made whenever needed and they will provide additional data to assess the behavior of tidal systems in the future. This information could be also considered by managers as a reliable tool in marsh creation and restoration projects. In fact, from a geomorphological point of view, restored marsh and channel systems rapidly develop up to the order of months, requiring high resolution and frequency of surveys. In particular, our study site well shows interesting results which might help management and design of future restoration projects. The methodology presented in this work can hence be replicated in any micro-tidal system in order to assess the response of restoration interventions to ordinary tide cycles and extreme events, both for geomorphology and vegetation tracking.

Further improvements of the research presented in this work is likely represented by the use of an aircraft with on-board RTK [71] that limits the need for a wide set of GCPs. The same DJI Phantom 3 Professional we used for the aerial surveys in this work is already available in a more recent version that integrates such a technology (DJI Phantom 4 RTK). Moreover, the advantages of GNSS kinematic modes are also available in post-processing [72] with a final centimeter-level accuracy and the acquisition of oblique images [73] leads to higher vertical accuracies. This can be a crucial aspect for improving and developing a precise monitoring of the mudflat. The combination of on-board RTK with oblique images is also able to provide consistent estimates not only for the exterior orientation, but also with regard to the interior orientation [74,75]. In fact, the accurate estimation of the focal length is crucial for achieving the best vertical accuracies [76], in particular when using UAV image datasets.

Finally, numerical simulations of hydro-dynamics and sediment transportation within such a small, but quite complex, tidal system, based on high-resolution elevation models will explain the driving factors of the morphological evolution enabling a better understanding of restoration interventions of salt marshes for a better management of coastal environments.

Author Contributions: Conceptualization, Y.T., A.P., L.W.S. and W.N.; methodology, Y.T., A.P. and W.N.; software, Y.T., A.P. and G.F.; validation, Y.T., A.P., L.W.S., J.C.S. and W.N.; formal analysis, Y.T. and A.P.; investigation, Y.T., A.P., C.C. and W.N.; resources, Y.T., A.P., G.F. and W.N.; data curation, C.C., G.F. and W.N.; writing—original draft preparation, Y.T. and W.N.; writing—review and editing, Y.T., A.P. and W.N.; visualization, Y.T.; supervision, A.P. and W.N.; project administration, A.P., L.W.S., J.C.S. and W.N.; funding acquisition, Y.T., A.P., G.F., L.W.S. and W.N. All authors have read and agreed to the published version of the manuscript.

Funding: This research was funded by Minigrant 2018-Salisbury University-Department of Mathematics and Computer Science.

Institutional Review Board Statement: Not applicable.

Informed Consent Statement: Not applicable.

Data Availability Statement: Not applicable.

Acknowledgments: The authors would like to thank (i) Maryland Department of Transportation–Maryland Port Administration, Maryland Environmental Service and United States Army Corps of Engineers for the provision of the as-built data of the cell and (ii) Alessandro Gerevini and Michela Quitadamo for the contribution during in-situ survey operations. Partial financial support for this research was provided by the Maryland Department of Transportation Maryland Port Administration with project management by the Maryland Environmental Service. Reviews by Michelle Osborn and Claire Ruark improved this manuscript. Partial financial support for this research was provided by the University of Ferrara with the mobility funds for Ph.D. students. This is contribution 5991 of the University of Maryland Center for Environmental Science–Horn Point Laboratory.

Conflicts of Interest: The authors declare no conflict of interest. The funders had no role in the design of the study; in the collection, analyses, or interpretation of data; in the writing of the manuscript, or in the decision to publish the results.

Abbreviations

The following abbreviations are used in this manuscript:

AGL	Above Ground Level
ASLR	Absolute Sea Level Rise
BBA	Bundle Block Adjustment
C-1B	Cell 1B
CB	Chesapeake Bay
CP	Check Point
DEM	Digital Elevation Model
DJI-P3P	DJI Phantom 3 Professional
DTM	Digital Terrain Model
GCP	Ground Control Point
GNSS	Global Navigation Satellite System
GSD	Ground Sample Distance
LiDAR	Light Detection And Ranging
MC	Main Channel
MDOT MPA	Maryland Department of Transportation–Maryland Port Administration
MES	Maryland Environmental Service
MVS	Multi-View-Stereo
NAD	North American Datum
NAVD	North American Vertical Datum
RGB	Red Green Blue
RMSE	Root Mean Square Error
RTK	Real-Time Kinematic
SC	Secondary Channel
SfM	Structure-from-Motion
SLR	Sea Level Rise
TLS	Terrestrial Laser Scanning
UAV	Unmanned Aerial Vehicle

USACE	United States Army Corps of Engineers
VP	Validation Point
WL	Water Level

References

- Dada, O.A.; Agbaje, A.O.; Adesina, R.B.; Asiwaju-Bello, Y.A. Effect of coastal land use change on coastline dynamics along the Nigerian Transgressive Mahin mud coast. *Ocean Coast. Manag.* **2019**, *168*, 251–264. [CrossRef]
- Thoai, D.T.; Dang, A.N.; Oanh, N.T.K. Analysis of coastline change in relation to meteorological conditions and human activities in Ca mau cape, Viet Nam. *Ocean Coast. Manag.* **2019**, *171*, 56–65. [CrossRef]
- Moffett, K.B.; Nardin, W.; Silvestri, S.; Wang, C.; Temmerman, S. Multiple Stable States and Catastrophic Shifts in Coastal Wetlands: Progress, Challenges, and Opportunities in Validating Theory Using Remote Sensing and Other Methods. *Remote Sens.* **2015**, *7*, 10184–10226. [CrossRef]
- Dean, R.; Houston, J. Determining shoreline response to sea level rise. *Coast. Eng.* **2016**, *114*, 1–8. [CrossRef]
- Carrasco, A.; Ferreira, Ó.; Roelvink, D. Coastal lagoons and rising sea level: A review. *Earth Sci. Rev.* **2016**, *154*, 356–368. [CrossRef]
- Alizad, K.; Hagen, S.C.; Medeiros, S.C.; Bilskie, M.V.; Morris, J.T.; Balthis, L.; Buckel, C.A. Dynamic responses and implications to coastal wetlands and the surrounding regions under sea level rise. *PLoS ONE* **2016**, *13*, e0205176. [CrossRef]
- Nardin, W.; Edmonds, D.; Fagherazzi, S. Influence of vegetation on spatial patterns of sediment deposition in deltaic islands during flood. *Adv. Water Resour.* **2016**, *93*, 236–248. [CrossRef]
- Nardin, W.; Larsen, L.; Fagherazzi, S.; Wiberg, P. Tradeoffs among hydrodynamics, sediment fluxes and vegetation community in the Virginia Coast Reserve, USA. *Estuar. Coast. Shelf Sci.* **2018**, *210*, 98–108. [CrossRef]
- Leonardi, N.; Carnacina, I.; Donatelli, C.; Ganju, N.K.; Plater, A.J.; Schuerch, M.; Temmerman, S. Dynamic interactions between coastal storms and salt marshes: A review. *Geomorphology* **2018**, *301*, 92–107. [CrossRef]
- Passeri, D.L.; Hagen, S.C.; Plant, N.G.; Bilskie, M.V.; Medeiros, S.C.; Alizad, K. Tidal hydrodynamics under future sea level rise and coastal morphology in the Northern Gulf of Mexico. *Earth's Future* **2016**, *4*, 159–176. [CrossRef]
- Alizad, K.; Hagen, S.C.; Morris, J.T.; Medeiros, S.C.; Bilskie, M.V.; Weishampel, J.F. Coastal wetland response to sea-level rise in a fluvial estuarine system. *Earth's Future* **2016**, *4*, 483–497. [CrossRef]
- Passeri, D.L.; Hagen, S.C.; Bilskie, M.V.; Medeiros, S.C. On the significance of incorporating shoreline changes for evaluating coastal hydrodynamics under sea level rise scenarios. *Nat. Hazards* **2015**, *75*, 1599–1617. [CrossRef]
- Reef, R.; Schuerch, M.; Christie, E.K.; Möller, I.; Spencer, T. The effect of vegetation height and biomass on the sediment budget of a European saltmarsh. *Estuar. Coast. Shelf Sci.* **2018**, *202*, 125–133. [CrossRef]
- Baustian, J.J.; Mendelsohn, I.A.; Hester, M.W. Vegetation's importance in regulating surface elevation in a coastal salt marsh facing elevated rates of sea level rise. *Glob. Chang. Biol.* **2012**, *18*, 3377–3382. [CrossRef]
- Broome, S.W.; Seneca, E.D.; Woodhouse, W.W. Tidal salt marsh restoration. *Aquat. Bot.* **1988**, *32*, 1–22. [CrossRef]
- Raposa, K.B.; Wasson, K.; Smith, E.; Crooks, J.A.; Delgado, P.; Fernald, S.H.; Ferner, M.C.; Helms, A.; Hice, L.A.; Mora, J.W.; et al. Assessing tidal marsh resilience to sea-level rise at broad geographic scales with multi-metric indices. *Biol. Conserv.* **2016**, *204*, 263–275. [CrossRef]
- Best, Ü.S.N.; Van der Wegen, M.; Dijkstra, J.; Willemsen, P.W.J.M.; Borsje, B.W.; Roelvink, D.J.A. Do salt marshes survive sea level rise? Modelling wave action, morphodynamics and vegetation dynamics. *Environ. Model. Softw.* **2018**, *109*, 152–166. [CrossRef]
- Morris, J.T.; Sundareshwar, P.V.; Nietch, C.T.; Kjerfve, B.; Cahoon, D.R. Responses of coastal wetlands to rising sea level. *Ecology* **2002**, *83*, 2869–2877. [CrossRef]
- Barbier, E.B.; Hacker, S.D.; Kennedy, C.; Koch, E.W.; Stier, A.C.; Silliman, B.R. The value of estuarine and coastal ecosystem services. *Ecol. Monogr.* **2011**, *81*, 169–193. [CrossRef]
- Schuerch, M.; Spencer, T.; Evans, B. Coupling between tidal mudflats and salt marshes affects marsh morphology. *Mar. Geol.* **2019**, *412*, 95–106. [CrossRef]
- Liu, Z.; Fagherazzi, S.; She, X.; Ma, X.; Xie, C.; Cui, B. Efficient tidal channel networks alleviate the drought-induced die-off of salt marshes: Implications for coastal restoration and management. *Sci. Total Environ.* **2020**, *749*, 141493. [CrossRef] [PubMed]
- Sallenger, A.H.; Doran, K.S.; Howd, P.A. Hotspot of accelerated sea-level rise on the Atlantic Coast of North America. *Nat. Clim. Chang.* **2012**, *2*, 884–888. [CrossRef]
- Lee, S.B.; Li, M.; Zhang, F. Impact of sea level rise on tidal range in Chesapeake and Delaware Bays. *J. Geophys. Res. Ocean.* **2017**, *122*, 3917–3938. [CrossRef]
- Xie, X.; Li, M.; Ni, W. Roles of Wind-Driven Currents and Surface Waves in Sediment Resuspension and Transport during a Tropical Storm. *J. Geophys. Res. Ocean.* **2018**, *123*, 8638–8654. [CrossRef]
- Boon, J.D.; Brubaker, J.M.; Forrest, D.R. Chesapeake bay land subsidence and sea level change: An evaluation of past and present trends and future outlook. In *Applied Marine Science and Ocean Engineering*; Special Report No. 425; Virginia Institute of Marine Science, William & Mary: Gloucester Point, VA, USA, 2010.
- USACE; Paul, S. Sarbanes Ecosystem Restoration Project at Poplar Island, Talbot County, MD—Fact Sheet as of 1 February 2019. U.S. Army Corps of Engineers—Baltimore District. 2019. Available online: <https://usace.contentdm.oclc.org/digital/collection/p16021coll11/id/3442> (accessed on 2 May 2019).

27. Fleri, J.R.; Lera, S.; Gerevini, A.; Staver, L.; Nardin, W. Empirical observations and numerical modelling of tides, channel morphology, and vegetative effects on accretion in a restored tidal marsh. *Earth Surf. Process. Landf.* **2019**. [[CrossRef](#)]
28. Le Cozannet, G.; Garcin, M.; Yates, M.; Idier, D.; Meyssignac, B. Approaches to evaluate the recent impacts of sea-level rise on shoreline changes. *Earth Sci. Rev.* **2014**, *138*, 47–60. [[CrossRef](#)]
29. Alesheikh, A.A.; Ghorbanali, A.; Nouri, N. Coastline change detection using remote sensing. *Int. J. Environ. Sci. Technol.* **2007**, *4*, 61–66. [[CrossRef](#)]
30. Burningham, H.; French, J. Understanding coastal change using shoreline trend analysis supported by cluster-based segmentation. *Geomorphology* **2017**, *282*, 131–149. [[CrossRef](#)]
31. Taddia, Y.; Corbau, C.; Zambello, E.; Russo, V.; Simeoni, U.; Russo, P.; Pellegrinelli, A. UAVS to assess the evolution of embryo dunes. *ISPRS Int. Arch. Photogramm. Remote Sens. Spat. Inf. Sci.* **2017**, *XLII-2/W6*, 363–369. [[CrossRef](#)]
32. Lowe, M.K.; Adnan, F.A.F.; Hamylton, S.M.; Carvalho, R.C.; Woodroffe, C.D. Assessing Reef-Island Shoreline Change Using UAV-Derived Orthomosaics and Digital Surface Models. *Drones* **2019**, *3*, 44. [[CrossRef](#)]
33. Westoby, M.; Brasington, J.; Glasser, N.; Hambrey, M.; Reynolds, J. ‘Structure-from-Motion’ photogrammetry: A low-cost, effective tool for geoscience applications. *Geomorphology* **2012**, *179*, 300–314. [[CrossRef](#)]
34. Mancini, F.; Dubbini, M.; Gattelli, M.; Stecchi, F.; Fabbri, S.; Gabbianelli, G. Using Unmanned Aerial Vehicles (UAV) for High-Resolution Reconstruction of Topography: The Structure from Motion Approach on Coastal Environments. *Remote Sens.* **2013**, *5*, 6880–6898. [[CrossRef](#)]
35. Gong, C.; Lei, S.; Bian, Z.; Liu, Y.; Zhang, Z.; Cheng, W. Analysis of the Development of an Erosion Gully in an Open-Pit Coal Mine Dump During a Winter Freeze-Thaw Cycle by Using Low-Cost UAVs. *Remote Sens.* **2019**, *11*, 1356. [[CrossRef](#)]
36. Niethammer, U.; James, M.; Rothmund, S.; Travelletti, J.; Joswig, M. UAV-based remote sensing of the Super-Sauze landslide: Evaluation and results. *Eng. Geol.* **2012**, *128*, 2–11. [[CrossRef](#)]
37. Hugenholtz, C.H.; Whitehead, K.; Brown, O.W.; Barchyn, T.E.; Moorman, B.J.; LeClair, A.; Riddell, K.; Hamilton, T. Geomorphological mapping with a small unmanned aircraft system (sUAS): Feature detection and accuracy assessment of a photogrammetrically-derived digital terrain model. *Geomorphology* **2013**, *194*, 16–24. [[CrossRef](#)]
38. Harwin, S.; Lucieer, A. Assessing the Accuracy of Georeferenced Point Clouds Produced via Multi-View Stereopsis from Unmanned Aerial Vehicle (UAV) Imagery. *Remote Sens.* **2012**, *4*, 1573–1599. [[CrossRef](#)]
39. Drummond, C.D.; Harley, M.D.; Turner, I.L.; AMatheen, A.N.; Glamore, W.C. UAV applications to coastal engineering. In Proceedings of the Australasian Coasts & Ports Conference 2015: 22nd Australasian Coastal and Ocean Engineering Conference and the 15th Australasian Port and Harbour Conference, Engineers Australia and IPENZ, Auckland, New Zealand, 15–18 September 2015; p. 267.
40. Turner, I.L.; Harley, M.D.; Drummond, C.D. UAVs for coastal surveying. *Coast. Eng.* **2016**, *114*, 19–24. [j.coastaleng.2016.03.011](#). [[CrossRef](#)]
41. Gonçalves, J.A.; Henriques, R. UAV photogrammetry for topographic monitoring of coastal areas. *ISPRS J. Photogramm. Remote Sens.* **2015**, *104*, 101–111. [[CrossRef](#)]
42. Scarelli, F.M.; Sistilli, F.; Fabbri, S.; Cantelli, L.; Barboza, E.G.; Gabbianelli, G. Seasonal dune and beach monitoring using photogrammetry from UAV surveys to apply in the ICZM on the Ravenna coast (Emilia-Romagna, Italy). *Remote Sens. Appl. Soc. Environ.* **2017**, *7*, 27–39. [[CrossRef](#)]
43. Taddia, Y.; Corbau, C.; Zambello, E.; Pellegrinelli, A. UAVs for Structure-From-Motion Coastal Monitoring: A Case Study to Assess the Evolution of Embryo Dunes over a Two-Year Time Frame in the Po River Delta, Italy. *Sensors* **2019**, *19*, 1717. [[CrossRef](#)] [[PubMed](#)]
44. Casella, E.; Rovere, A.; Pedroncini, A.; Stark, C.P.; Casella, M.; Ferrari, M.; Firpo, M. Drones as tools for monitoring beach topography changes in the Ligurian Sea (NW Mediterranean). *Geo Mar. Lett.* **2016**, *36*, 151–163. [[CrossRef](#)]
45. Nikolakopoulos, K.G.; Kozarski, D.; Kogkas, S. Coastal areas mapping using UAV photogrammetry. *Earth Resour. Environ. Remote Sens. Gis Appl. VIII* **2017**, *10428*, 23. [[CrossRef](#)]
46. Torres-Freyermuth, A.; Medellín, G.; Mendoza, E.T.; Ojeda, E.; Salles, P. Morphodynamic Response to Low-Crested Detached Breakwaters on a Sea Breeze-Dominated Coast. *Water* **2019**, *11*, 635. [[CrossRef](#)]
47. Watanabe, Y.; Kawahara, Y. UAV Photogrammetry for Monitoring Changes in River Topography and Vegetation. *Procedia Eng.* **2016**, *154*, 317–325. [[CrossRef](#)]
48. Rossini, M.; Mauro, B.D.; Garzonio, R.; Baccolo, G.; Cavallini, G.; Mattavelli, M.; Amicis, M.D.; Colombo, R. Rapid melting dynamics of an alpine glacier with repeated UAV photogrammetry. *Geomorphology* **2018**, *304*, 159–172. [[CrossRef](#)]
49. Immerzeel, W.; Kraaijenbrink, P.; Shea, J.; Shrestha, A.; Pellicciotti, F.; Bierkens, M.; de Jong, S. High-resolution monitoring of Himalayan glacier dynamics using unmanned aerial vehicles. *Remote Sens. Environ.* **2014**, *150*, 93–103. [[CrossRef](#)]
50. Thiebes, B.; Tomelleri, E.; Mejia-Aguilar, A.; Rabanser, M.; Schlögel, R.; Mulas, M.; Corsini, A. Assessment of the 2006 to 2015 Corvara landslide evolution using a UAV-derived DSM and orthophoto. In Proceedings of the 12th International Symposium on Landslides, Naples, Italy, 12–19 June 2016. [[CrossRef](#)]
51. Hu, S.; Qiu, H.; Wang, X.; Gao, Y.; Wang, N.; Wu, J.; Yang, D.; Cao, M. Acquiring high-resolution topography and performing spatial analysis of loess landslides by using low-cost UAVs. *Landslides* **2018**, *15*, 593–612. [[CrossRef](#)]
52. Murtiyoso, A.; Grussenmeyer, P. Documentation of heritage buildings using close-range UAV images: Dense matching issues, comparison and case studies. *Photogramm. Rec.* **2017**, *32*, 206–229. [[CrossRef](#)]

53. Russo, M.; Carnevali, L.; Russo, V.; Savastano, D.; Taddia, Y. Modeling and deterioration mapping of façades in historical urban context by close-range ultra-lightweight UAVs photogrammetry. *Int. J. Archit. Herit.* **2019**, *13*, 549–568. [CrossRef]
54. Cook, K.L. An evaluation of the effectiveness of low-cost UAVs and structure from motion for geomorphic change detection. *Geomorphology* **2017**, *278*, 195–208. [CrossRef]
55. Clapuyt, F.; Vanacker, V.; Oost, K.V. Reproducibility of UAV-based earth topography reconstructions based on Structure-from-Motion algorithms. *Geomorphology* **2016**, *260*, 4–15. [CrossRef]
56. James, M.; Robson, S.; d'Oleire Oltmanns, S.; Niethammer, U. Optimising UAV topographic surveys processed with structure-from-motion: Ground control quality, quantity and bundle adjustment. *Geomorphology* **2017**, *280*, 51–66. [CrossRef]
57. Jaud, M.; Grasso, F.; Le Dantec, N.; Verney, R.; Delacourt, C.; Ammann, J.; Deloffre, J.; Grandjean, P. Potential of UAVs for Monitoring Mudflat Morphodynamics (Application to the Seine Estuary, France). *ISPRS Int. J. Geo Inf.* **2016**, *5*, 50. [CrossRef]
58. Taddia, Y.; Nardin, W.; Corbau, C.; Franchi, G.; Stevenson, C.J.; Staver, L.W., Channels' shape evolution detected by uavs in a restored salt marsh. In *Coastal Sediments 2019*; World Scientific: Singapore, 2019; pp. 1519–1527. [CrossRef]
59. DJI. *Phantom 3 Professional User Manual v1.8*. Available online: <https://www.dji.com/it/phantom-3-pro/info> (accessed on 24 January 2018).
60. Agisoft. *Agisoft Metashape User Manual, Professional Edition, Version 1.5*. 2019. Available online: https://www.agisoft.com/pdf/metashape-pro_1_5_en.pdf (accessed on 18 February 2021).
61. Medeiros, S.; Hagen, S.; Weishampel, J.; Angelo, J. Adjusting Lidar-Derived Digital Terrain Models in Coastal Marshes Based on Estimated Aboveground Biomass Density. *Remote Sens.* **2015**, *7*, 3507–3525. [CrossRef]
62. Chassereau, J.E.; Bell, J.M.; Torres, R. A comparison of GPS and lidar salt marsh DEMs. *Earth Surf. Process. Landf.* **2011**, *36*, 1770–1775. [CrossRef]
63. Morris, J.T.; Porter, D.; Neet, M.; Noble, P.A.; Schmidt, L.; Lapine, L.A.; Jensen, J.R. Integrating LIDAR elevation data, multi-spectral imagery and neural network modelling for marsh characterization. *Int. J. Remote Sens.* **2005**, *26*, 5221–5234. [CrossRef]
64. Wulder, M.A.; Hall, R.J.; Coops, N.C.; Franklin, S.E. High Spatial Resolution Remotely Sensed Data for Ecosystem Characterization. *BioScience* **2004**, *54*, 511. [CrossRef]
65. Reed, D.J. The response of coastal marshes to sea-level rise: Survival or submergence? *Earth Surf. Process. Landf.* **1995**, *20*, 39–48. [CrossRef]
66. Fagherazzi, S.; Mariotti, G.; Leonardi, N.; Canestrelli, A.; Nardin, W.; Kearney, W.S. Salt Marsh Dynamics in a Period of Accelerated Sea Level Rise. *J. Geophys. Res. Earth Surf.* **2020**, *125*, e2019JF005200. [CrossRef]
67. Pinton, D.; Canestrelli, A.; Wilkinson, B.; Ifju, P.; Ortega, A. A new algorithm for estimating ground elevation and vegetation characteristics in coastal salt marshes from high-resolution UAV-based LiDAR point clouds. *Earth Surf. Process. Landf.* **2020**, *45*, 3687–3701. [CrossRef]
68. Parker, B.; Milbert, D.; Hess, K.; Gill, S. Integrating bathymetry, topography, and shoreline, and the importance of vertical datums. In *Oceans 2003. Celebrating the Past ... Teaming toward the Future*; (IEEE Cat. No.03CH37492); IEEE: San Diego, CA, USA, 2003; Volume 2, pp. 758–764. [CrossRef]
69. Marani, M.; Lanzoni, S.; Zandolin, D.; Seminara, G.; Rinaldo, A. Tidal meanders. *Water Resour. Res.* **2002**, *38*, 7–1–7–14. [CrossRef]
70. Belliard, J.P.; Marco, N.D.; Carniello, L.; Toffolon, M. Sediment and vegetation spatial dynamics facing sea-level rise in microtidal salt marshes: Insights from an ecogeomorphic model. *Adv. Water Resour.* **2016**, *93*, 249–264. [CrossRef]
71. Forlani, G.; Dall'Asta, E.; Diotri, F.; Cella, U.M.D.; Roncella, R.; Santise, M. Quality Assessment of DSMs Produced from UAV Flights Georeferenced with On-Board RTK Positioning. *Remote Sens.* **2018**, *10*, 311. [CrossRef]
72. Taddia, Y.; Stecchi, F.; Pellegrinelli, A. Coastal Mapping Using DJI Phantom 4 RTK in Post-Processing Kinematic Mode. *Drones* **2020**, *4*, 9. [CrossRef]
73. Jiang, S.; Jiang, W. Efficient SfM for Oblique UAV Images: From Match Pair Selection to Geometrical Verification. *Remote Sens.* **2018**, *10*, 1246. [CrossRef]
74. Taddia, Y.; Stecchi, F.; Pellegrinelli, A. Using dji phantom 4 rtk drone for topographic mapping of coastal areas. *ISPRS Int. Arch. Photogramm. Remote Sens. Spat. Inf. Sci.* **2019**, *XLII-2/W13*, 625–630. [CrossRef]
75. Tomaštk, J.; Mokroš, M.; Surový, P.; Grznárová, A.; Merganič, J. UAV RTK/PPK Method—An Optimal Solution for Mapping Inaccessible Forested Areas? *Remote Sens.* **2019**, *11*, 721. [CrossRef]
76. Harwin, S.; Lucieer, A.; Osborn, J. The Impact of the Calibration Method on the Accuracy of Point Clouds Derived Using Unmanned Aerial Vehicle Multi-View Stereopsis. *Remote Sens.* **2015**, *7*, 11933–11953. [CrossRef]